

Dust mass in protoplanetary disks with porous dust opacities

Yao Liu^{1,2}, H el ene Roussel³, Hendrik Linz⁴, Min Fang², Sebastian Wolf⁵, Florian Kirchschlager⁶, Thomas Henning⁴,
Haifeng Yang⁷, Fujun Du², Mario Flock⁴, and Hongchi Wang²

¹ School of Physical Science and Technology, Southwest Jiaotong University, Chengdu 610031, China;
e-mail: yliu@swjtu.edu.cn

² Purple Mountain Observatory, Chinese Academy of Sciences, 10 Yuanhua Road, Nanjing 210023, China

³ Institut d'Astrophysique de Paris, Sorbonne Universit e, CNRS (UMR7095), 75014 Paris, France

⁴ Max-Planck-Institut f ur Astronomie, K onigstuhl 17, D-69117 Heidelberg, Germany

⁵ Institut f ur Theoretische Physik und Astrophysik, Christian-Albrechts-Universit at zu Kiel, Leibnizstr. 15, 24118 Kiel, Germany

⁶ Sterrenkundig Observatorium, Ghent University, Krijgslaan 281-S9, B9000 Gent, Belgium

⁷ Institute for Astronomy, School of Physics, Zhejiang University, 866 Yu Hang Tang Road, Hangzhou, Zhejiang 310027, China

Preprint online version: November 4, 2024

ABSTRACT

Atacama Large Millimeter/submillimeter Array surveys have suggested that protoplanetary disks are not massive enough to form the known exoplanet population, under the assumption that the millimeter continuum emission is optically thin. In this work, we investigate how the mass determination is influenced when the porosity of dust grains is considered in radiative transfer models. The results show that disks with porous dust opacities yield similar dust temperature, but systematically lower millimeter fluxes compared to disks incorporating compact dust grains. Moreover, we recalibrate the relation between dust temperature and stellar luminosity for a wide range of stellar parameters, and calculate the dust masses of a large sample of disks using the traditionally analytic approach. The median dust mass from our calculation is about 6 times higher than the literature result, and this is mostly driven by the different opacities of porous and compact grains. A comparison of the cumulative distribution function between disk dust masses and exoplanet masses show that the median exoplanet mass is about 2 times lower than the median dust mass, if grains are porous, and there are no exoplanetary systems with masses higher than the most massive disks. Our analysis suggests that adopting porous dust opacities may alleviate the mass budget problem for planet formation. As an example illustrating the combined effects of optical depth and porous dust opacities on the mass estimation, we conduct new IRAM/NIKA-2 observations toward the IRAS 04370+2559 disk and perform a detailed radiative transfer modeling of the spectral energy distribution. The best-fit dust mass is roughly 100 times higher than the value from the traditionally analytic calculation. Future spatially resolved observations at various wavelengths are required to better constrain the dust mass.

Key words. circumstellar matter – planetary systems: protoplanetary disks – radiative transfer – facilities: IRAM

1. Introduction

Dust grains, though occupying only about 1% of the total disk mass, is a crucial ingredient that influences many aspects of disk evolution and planet formation (e.g., Natta et al. 2007; Birnstiel 2023). First, dust opacity dominates over gas opacity, therefore dust grains play an important role in setting the thermal and geometrical structure of disks. Secondly, dust particles provide the surface area on which complex chemical reactions take place (e.g., Garrod & Herbst 2006; Henning & Semenov 2013;  berg et al. 2023), and also act as carriers to redistribute volatile species within the disk via dust diffusion, settling and radial drift (e.g., Krijt et al. 2016; Stammer et al. 2017; Eistrup & Henning 2022). Finally, dust grains are the building blocks for the formation of planetesimals, terrestrial planets, and the cores of giant planets. Consequently, the total amount of dust content is one of the paramount properties that characterize the potential for planet formation.

Estimating dust mass is commonly accomplished by millimeter continuum observations. Thanks to the high sensitivity of the Atacama Large Millimeter/submillimeter Array (ALMA), a large sample of about 1,000 disks located in nearby star-forming regions have been observed at millimeter wavelengths, (e.g., Ansdell et al. 2016; Barenfeld et al. 2016; Pascucci et al. 2016;

Cazzoletti et al. 2019; Tazzari et al. 2021; Grant et al. 2021). Assuming the emitting dust is optically thin and isothermal, the measured flux density F_ν can be converted into dust masses via the analytic formula

$$M_{\text{dust}} = \frac{F_\nu D^2}{\kappa_\nu B_\nu(T_{\text{dust}})}, \quad (1)$$

where $B_\nu(T_{\text{dust}})$ stands for the Planck function given at the observed frequency ν and dust temperature T_{dust} , D refers to the distance to the object, and κ_ν is the mass absorption coefficient. Based on Eq. 1, Andrews (2020) build the cumulative distribution function (CDF) of M_{dust} for 887 disks, and find that less than ~10% disks have enough material to produce our solar system or its analogs in the exoplanet population. Similarly, Manara et al. (2018) find that exoplanetary systems masses are comparable or even higher than the most massive disks with ages of ~1 – 3 Myr. Although the discrepancy between the disk and exoplanets mass distributions is mitigated by accounting for observational selection and detection biases (Mulders et al. 2021), the findings by Andrews (2020) and Manara et al. (2018) naturally raise a conundrum that protoplanetary disks do not have enough mass to make planetary systems. This puzzle is referred as the ‘‘mass budget problem’’ of planet formation in the literature.

Proposed solutions have been considered in three scenarios. The first scenario suggests that planet formation might begin at earlier stages of disk evolution than previously thought. The prevalence of substructures in protostellar disks is the supporting evidence (Segura-Cox et al. 2020; Sheehan et al. 2020; Ohashi et al. 2023; Hsieh et al. 2024), since disk substructures may be created by planets (Kley & Nelson 2012; Paardekooper et al. 2023). Moreover, young disks in the Class 0/I phases are generally more massive than Class II disks (Tychoniec et al. 2018, 2020), providing more material for planet formation. The second scenario assumes that the disk acts as a conveyor belt that transports material from the environment to the central star (Manara et al. 2018; Gupta et al. 2023, 2024). Thus, the total amount of material available for planet formation actually exceeds the observed value. The third proposal argues that M_{dust} estimated using Eq. 1 is merely a lower limit (e.g., Ballering & Eisner 2019), because protoplanetary disks are not necessarily optically thin at millimeter wavelengths (e.g., Liu et al. 2017; Rilinger et al. 2023; Xin et al. 2023). Recently, Savvidou & Bitsch (2024) show that the early formation of giant planets is expected to create pressure bumps exterior to the planetary orbit, which will trap the inward drifting dust. The trapped dust will be largely unaccounted for by the approximation of optically thin emission. Assuming dust grains are compact spheres, Liu et al. (2022) demonstrate that the disk outer radius, inclination, and true dust mass are most important to create optically thick regions, resulting in mass underestimations from a few to hundreds times.

Theoretical studies show that dust grains in protoplanetary disks might be porous in the process of coagulation and growth (e.g., Dominik & Tielens 1997; Wurm & Blum 1998), and grain growth via porous aggregates can overcome the radial drift barrier to form planetesimals (Okuzumi et al. 2012; Kataoka et al. 2013; Michoulier et al. 2024). The existence of porous dust grains is observationally supported. Near-infrared scattered light observations show that the polarization phase functions are consistent with model predictions incorporating micron-sized porous dust grains (e.g., Stolker et al. 2016; Ginski et al. 2023; Tazaki et al. 2023). A detailed analysis of multiwavelength continuum and millimeter polarization observations of the HL Tau disk indicates that dust grains are porous, and the porosity ranges from 70% to 97% depending on the best-fit grain size (Zhang et al. 2023).

The absorption/scattering coefficients of porous dust grains are different from those of compact spherical particles (e.g., Kirchschrager & Wolf 2014; Ysard et al. 2018; Kirchschrager et al. 2019), which have a direct impact on the radiative transfer process in protoplanetary disks. In this work, using self-consistent radiative transfer models, we investigate how porous dust opacities influence the dust temperature, emergent millimeter flux and therefore the estimation of M_{dust} . The setup of the radiative transfer models and the resulting trends are presented in Sect. 2. In Sect. 3, we apply porous dust opacities to the calculation of M_{dust} for a large number of disks, and compare the CDF between the disk sample and the exoplanet population investigated by Mulders et al. (2021). As an application, we model the spectral energy distribution (SED) of the IRAS 04370+2559 disk in Sect. 4. The paper concludes with a summary in Sect. 5.

2. Radiative transfer models

In this section, we first give an introduction about the setup of the radiative transfer model, and then build a grid of models by sampling a few key parameters that have prominent effects on the dust temperature and millimeter flux.

2.1. Dust density structure

We consider a flared disk that includes two distinct dust grain populations, i.e., a small grain population (SGP) and a large grain population (LGP). We fix the disk inner radius R_{in} to 0.1 AU that is close to the dust sublimation radius of a typical T Tauri star. The SGP occupies a small fraction of the dust mass, $(1 - f) M_{\text{dust}}$, and its scale height follows a power law

$$h = h_{100} \times \left(\frac{R}{100 \text{ AU}} \right)^{\Psi}. \quad (2)$$

The flaring index is denoted with Ψ , and h_{100} refers to the scale height at a radial distance of $R = 100$ AU. On the contrary, the LGP which has a mass of $f M_{\text{dust}}$ dominates the dust mass, and is concentrated close to the midplane with a scale height of Λh . The degree of dust settling is characterized by setting $\Lambda = 0.2$ (Andrews et al. 2011). To distribute the mass for the SGP and LGP, we adopt $f = 0.85$ that is a typical value found from multiwavelength modeling of protoplanetary disks (e.g., Andrews et al. 2011; van der Marel et al. 2018; Schwarz et al. 2021; Zhang et al. 2021). The dust surface density is assumed to be a power law with an exponential taper

$$\Sigma(R) = \Sigma_c \left(\frac{R}{R_c} \right)^{-\gamma} \exp \left[- \left(\frac{R}{R_c} \right)^{2-\gamma} \right], \quad (3)$$

where γ is the gradient parameter, and R_c is a characteristic radius. This is the similarity solution for disk evolution, which assume that the viscosity has a power-law radial dependence and is independent of time (Lynden-Bell & Pringle 1974). The proportionality factor Σ_c is determined by normalizing the total dust mass M_{dust} . We truncate the disk at an outer radius of $8 R_c$. The dust volume density is parameterized as

$$\rho_{\text{SGP}}(R, z) = \frac{(1-f)\Sigma(R)}{\sqrt{2\pi}h} \exp \left[- \frac{1}{2} \left(\frac{z}{h} \right)^2 \right], \quad (4)$$

$$\rho_{\text{LGP}}(R, z) = \frac{f\Sigma(R)}{\sqrt{2\pi}\Lambda h} \exp \left[- \frac{1}{2} \left(\frac{z}{\Lambda h} \right)^2 \right]. \quad (5)$$

Table 1 summarizes the parameters of the model.

2.2. Dust properties

The dust ensemble is composed of water ice (Warren & Brandt 2008), astronomical silicates (Draine 2003), troilite (Henning & Stognienko 1996), and refractory organic material (Henning & Stognienko 1996), with volume fractions being 36%, 17%, 3%, and 44%, respectively. The optical constants of each individual are mixed using the Bruggeman mixing rule (Bruggeman 1935). The resulting optical constants are referred as the DSHARP dust model (Birnstiel et al. 2018). The bulk density of the mix is $\rho_{\text{s,compact}} = 1.675 \text{ g/cm}^3$. To have porous grains, we adopt the effective medium theory (EMT), and mix the DSHARP dust composition with vacuum using the Bruggeman mixing rule. The mixed complex refractive indices are used to calculate dust absorption/scattering properties with the Mie theory and OpTool (Dominik et al. 2021). The porosity \mathcal{P} controls the volume fraction of vacuum. We choose $\mathcal{P} = 0.8$, a value consistent with current observations of protoplanetary disks (e.g., Zhang et al. 2023) and also derived for the cometary nucleus 67P/Churyumov–Gerasimenko (Kofman et al. 2015; Jorda et al. 2016). The bulk density of the porous dust grains

Table 1. Fixed and varied parameters of the model grid.

Parameter	Min	Max	Number	Sampling
T_\star [K]	3778	3778	1	fixed
L_\star [L_\odot]	0.86	0.86	1	fixed
R_{in} [AU]	0.1	0.1	1	fixed
γ	1.0	1.0	1	fixed
Λ	0.2	0.2	1	fixed
f	0.85	0.85	1	fixed
i [°]	30	30	1	fixed
$a_{\text{min}}^{\text{eff}}$ [μm]	0.01	0.01	1	fixed
$a_{\text{max.SGP}}^{\text{eff}}$ [μm]	1.0	1.0	1	fixed
$a_{\text{max.LGP}}^{\text{eff}}$ [mm]	1.0	1.0	1	fixed
R_c [AU]	5	200	10	logarithmic
Ψ	1.05	1.25	9	linear
h_{100} [AU]	4	18	8	linear
M_{dust} [M_\odot]	1×10^{-5}	1×10^{-2}	13	logarithmic

is $\rho_{\text{s,porous}} = (1 - \mathcal{P})\rho_{\text{s,compact}} = 0.335 \text{ g/cm}^3$. Note that compact dust particles can be considered as a limiting case of $\mathcal{P} = 0$.

We define an effective radius that is the radius of a volume-equivalent solid sphere, $a_{\text{eff}} = a(1 - \mathcal{P})^{1/3}$, where a is the grain size. In this work, we compare compact dust opacities with porous dust opacities assuming that both types of dust grains have the same effective radius a_{eff} . In the literature, the characteristic radius $a_c = a(1 - \mathcal{P})$ is another choice for describing the size-dependent dust opacities (Tazaki et al. 2019a; Zhang et al. 2023). For $\mathcal{P} = 0.8$, a_{eff} and a_c differ by a factor of ~ 3 . The effective grain size distribution follows the power law $dn(a_{\text{eff}}) \propto a_{\text{eff}}^{-3.5} da_{\text{eff}}$ with a minimum effective grain size fixed to $a_{\text{min}}^{\text{eff}} = 0.01 \mu\text{m}$. For the SGP, the maximum effective grain size is set to $a_{\text{max}}^{\text{eff}} = 1 \mu\text{m}$. For the LGP, we adopt $a_{\text{max}}^{\text{eff}} = 1 \text{ mm}$ accounting for grain growth commonly identified in protoplanetary disks. The porosity may not be uniform due to the dust coagulation of the SGP into the LGP. However, we focus only on the simplest scenario where the SGP and LGP are assumed to have the same porosity of $\mathcal{P} = 0.8$.

The panel (a) of Figure 1 shows the mass absorption coefficient at 1.3 mm ($\kappa_{1.3\text{mm}}$) as a function of $a_{\text{max}}^{\text{eff}}$. As can be seen, $\kappa_{1.3\text{mm}}$ of porous grains is lower than that of compact grains¹. For $a_{\text{max}}^{\text{eff}} = 1 \text{ mm}$, porous grains feature $\kappa_{1.3\text{mm}} = 0.37 \text{ cm}^2/\text{g}$ that is five times lower than compact grains with $\kappa_{1.3\text{mm}} = 1.86 \text{ cm}^2/\text{g}$, which will have a direct impact on the mass estimation, see Eq. 1. The differences in κ_ν between porous grains and compact grains are less pronounced in the optical regime, see panel (c) of Figure 1. This implies that T_{dust} obtained from the radiative transfer simulation will not differ too much between the two types of grains because most of the stellar energy emits at optical wavelengths. The opacity slope, e.g., $\beta_{1.3-3\text{mm}}$ measured between 1.3 mm and 3 mm, behaves differently between compact grains and porous grains. For compact grains, there is a peak around $a_{\text{max}}^{\text{eff}} \sim \lambda/2\pi$ due to the unique feature of Mie interference. For larger grain sizes, the opacity slope monotonically decreases with $a_{\text{max}}^{\text{eff}}$. If the dust emission is optically thin

¹ When the particle sizes are in the Rayleigh limit, fluffy grains can have increased dust opacities at millimeter wavelengths compared to compact grains with the same mass, and the increase is highly dependent on the dust composition (e.g., Stognienko et al. 1995; Henning & Stognienko 1996).

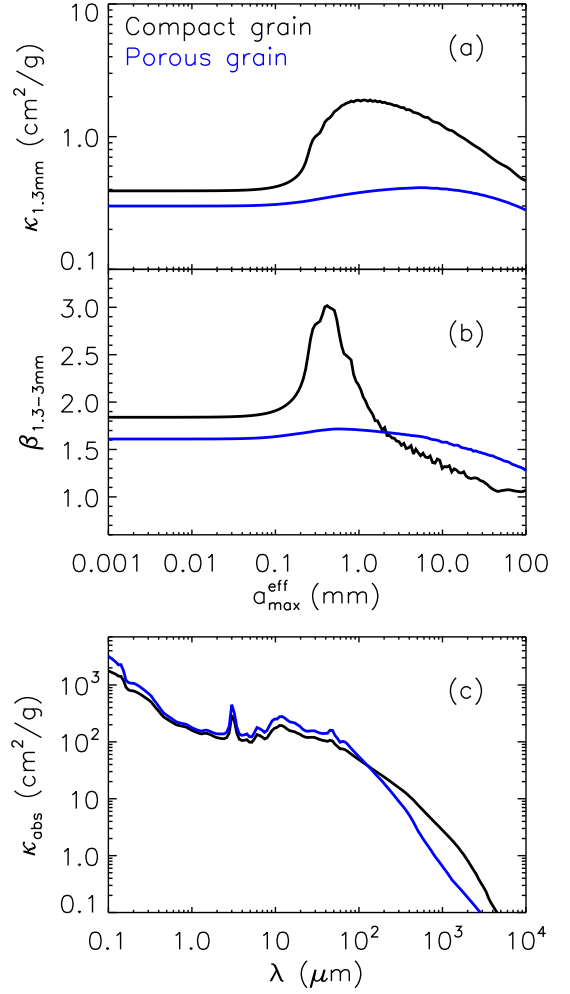


Fig. 1. Dust properties considered in this work. *Panel (a):* mass absorption coefficient at $\lambda = 1.3 \text{ mm}$ as a function of $a_{\text{max}}^{\text{eff}}$. *Panel (b):* opacity slope $\beta_{1.3-3\text{mm}}$ between 1.3 mm and 3 mm. The grain size distribution follows a power law $dn(a_{\text{eff}}) \propto a_{\text{eff}}^{-3.5} da_{\text{eff}}$ with a fixed $a_{\text{min}}^{\text{eff}} = 0.01 \mu\text{m}$. *Panel (c):* mass absorption coefficient as a function of wavelength for $a_{\text{max}}^{\text{eff}} = 1 \text{ mm}$. The black lines show the result for compact grains, whereas the case for the porous grains with a porosity of $\mathcal{P} = 0.8$ is indicated with blue lines.

and in the Rayleigh–Jeans tail, the opacity slope is linked to millimeter spectral indices (α) via $\beta = \alpha - 2$. This is the reason why dust grain sizes can be probed by multiwavelength millimeter observations (e.g., Ricci et al. 2010; Williams & Cieza 2011). However, if the dust particles are porous, the grain size becomes difficult to be constrained because the opacity slope is less sensitive to $a_{\text{max}}^{\text{eff}}$, see panel (b) of Figure 1 or Figure 3 in Miotello et al. (2023).

As described above, we modeled the porosity as a certain percentage of vacuum inclusion in dust grains by using the EMT, and calculated the dust properties with the Mie theory. A more sophisticated approach is to define the porosity by a size of void inclusion and a volume filling factor (e.g., Kirchsclager & Wolf 2014; Kirchsclager et al. 2019). In this way, dust properties of porous grains can be calculated with the DDSCAT code (Draine & Flatau 1994, 2010) by applying the discrete dipole approximation (Purcell & Pennypacker 1973). Kirchsclager & Wolf (2013) showed that absorption cross sections of micron-sized

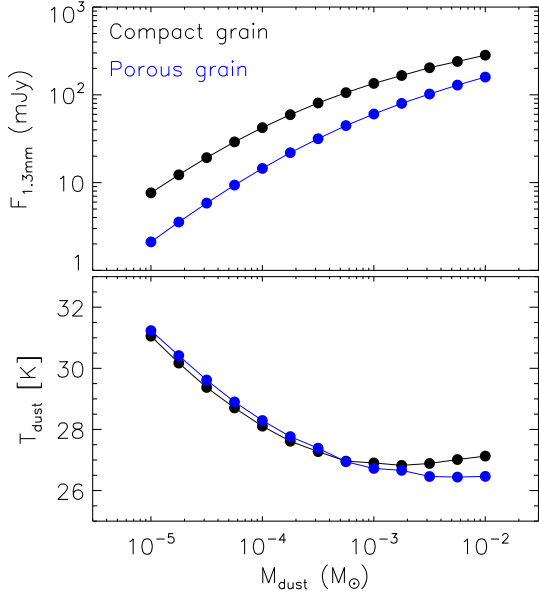


Fig. 2. Comparison of $F_{1.3\text{mm}}$ (upper panel) and T_{dust} (bottom panel) between models that use compact dust opacities (black) and porous dust opacities (blue), respectively. In the models, all of other parameters are fixed: $R_c = 30$ AU, $\Psi = 1.15$, $H_{100} = 10$ AU.

grains calculated with the Mie theory and DDSCAT code differ for $\lambda < 0.2 \mu\text{m}$ and $\lambda > 20 \mu\text{m}$. Comparisons for millimeter-sized grains are difficult, because running the DDSCAT code for grains with large size parameters ($2\pi a/\lambda$) is time-consuming, and the reliability of results needs to be validated as well. Hence, we leave it as a future direction to investigate the difference in the dust temperature between the two approaches, and how it would impact the estimation of dust mass.

2.3. Heating mechanisms

Stellar irradiation and viscous accretion are the major heating sources of protoplanetary disks. Viscous heating mainly affects the temperature distribution in the interior portion of the inner disk, e.g., $R \lesssim 2$ AU (Hartmann 2009; Harsono et al. 2015). However, the main disk mass reservoir is in the cold outer disk. Therefore, we only consider stellar irradiation in the simulation.

In Sect. 4, we will perform a detailed fitting to the SED of IRAS 04370+2559 that is a T Tauri star located in the Taurus star formation region. For convenience, we adopt its stellar luminosity and effective temperature ($L_\star = 0.86 L_\odot$, $T_{\text{eff}} = 3778$ K, see Sect. 4.1) in the establishment of the model grid. We take the distance of $D = 140$ pc to scale the simulated observable. We note that using different stellar properties will not have a significant impact on the trends of T_{dust} and millimeter F_ν with parameters explored in this work. The stellar spectrum is taken from the BT-Settl database (Allard et al. 2011), assuming a surface gravity of $\log g = 3.5$ and solar metallicity.

2.4. Establishment of the model grid

To build a grid of models, we explore a few key parameters that are expected to have the most significant impact on T_{dust} and the millimeter flux F_ν . The flaring index Ψ and scale height h_{100} work together to determine the disk geometry, therefore to alter

the total amount of stellar energy absorbed by the disk, which in turn affects T_{dust} and F_ν . As shown by Liu et al. (2022), the true M_{dust} , disk size and disk inclination (i) are most important to create optically thick regions. Accordingly, M_{dust} and R_c have an impact on the mass estimation. The disk inclination affects the optical depth along the line of sight, and therefore alters the millimeter F_ν . We refer to Liu et al. (2022) for details about the role of this parameter in determining the dust mass. For simplicity, we fixed $i = 30^\circ$ throughout this work.

We sample the above-mentioned four parameters (Ψ , h_{100} , M_{dust} and R_c) within reasonable ranges that are consistent with results derived from multiwavelength observations and modeling of protoplanetary disks (e.g., Andrews et al. 2011; Kirchschrager et al. 2016; Andrews et al. 2013; Liu et al. 2019). For parameters having a large dynamical range, the sampling is performed in a logarithmic manner, whereas parameters with a narrow dynamical range are sampled in the linear space. The grid points in each dimension are tabulated in Table 1. There are 9,360 models in total. We separately run the simulations using the compact dust opacities and porous dust opacities.

The well-tested RADMC-3D² package is invoked to solve the problem of continuum radiative transfer (Dullemond et al. 2012). Dust scattering is taken into account since literature works have demonstrated that it can reduce the emission from optically thick regions (Zhu et al. 2019; Sierra & Lizano 2020), and influence the millimeter spectral index (Liu 2019). We first run the thermal Monte-Carlo simulation, from which the mass-averaged dust temperature T_{dust} is obtained. Then, we simulate the flux densities from optical to millimeter wavelengths and the 0.88 mm images. The 0.88 mm images are used to derive an effective disk radius that is the radius at which a given fraction of the cumulative flux is contained. Following Tripathi et al. (2017), we compute the radius encircling 68% of the total flux, and compare our results with those measured on observed millimeter images of Taurus disks (Hendler et al. 2020).

2.5. Results

Figure 2 shows the mass-averaged dust temperature (T_{dust}) and flux density at 1.3 mm ($F_{1.3\text{mm}}$) as a function of M_{dust} . The difference in T_{dust} between compact dust opacities and porous dust opacities is less than ~ 1 K. In self-consistent radiative transfer modeling, only upper disk layers are directly illuminated by the central star, resulting in hot/warm upper disk layers. Generally, such hot/warm disk regions lie above the disk photosphere where the radial optical depth at $0.55 \mu\text{m}$ equals to unity, i.e., $\tau_{\text{radial},0.55 \mu\text{m}} = 1$, which is indicated with the grey lines in Figure 3. The interior disk regions are indirectly heated by both the radiation that is scattered from above towards the mid-plane and the reemission of the hot/warm layers. The former heating mechanism is mainly relevant to the optical cross section, while the infrared cross section is important for the latter heating process. As shown in panel (c) of Figure 1, porous dust grains feature higher optical cross sections, leading to a lower T_{dust} . However, porous dust grains also have larger infrared cross sections. Hot/warm layers will re-emit more infrared emission, and therefore compensate the reduced T_{dust} . These facts explain the small difference in T_{dust} between both types of dust grains. Models with porous dust opacities produce systematically lower $F_{1.3\text{mm}}$ than those with compact dust opacities. This is driven by the difference in the dust opacity, see panel (a) of Figure 1. For

² <http://www.ita.uni-heidelberg.de/~dullemond/software/radmc-3d/>.

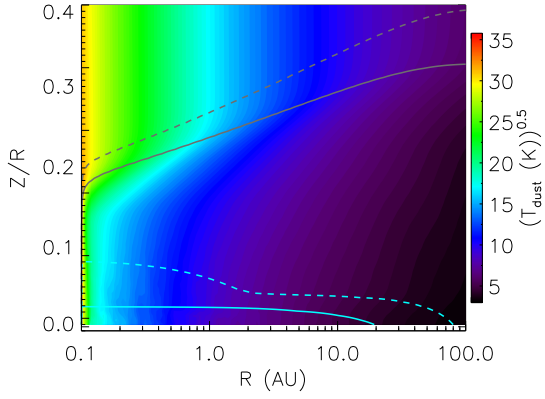


Fig. 3. Dust temperature of a representative model with parameters of $M_{\text{dust}} = 10^{-4} M_{\odot}$, $R_c = 30$ AU, $\Psi = 1.15$ and $H_{100} = 10$ AU. For a better representation, we show the quantity $\sqrt{T_{\text{dust}}}$. The grey solid line refers to the surface of radial optical depth at $\lambda = 0.55 \mu\text{m}$ being unity, i.e., $\tau_{\text{radial},0.55 \mu\text{m}} = 1$. This contour marks the disk photosphere where stellar photons are absorbed, and hence plays a crucial role in setting up the temperature structure. The cyan solid line shows the surface of vertical optical depth at $\lambda = 1.3$ mm being unity, i.e., $\tau_{\text{vertical},1.3 \text{ mm}} = 1$. This curve generally reflects the layer above which millimeter continuum emission can reach the observer viewed at a face-on orientation. For comparison, the grey dashed line and cyan dashed line show the same contours for a more massive disk with $M_{\text{dust}} = 3 \times 10^{-3} M_{\odot}$.

each of the 9,360 models in the grid, we calculate the ratio of $F_{1.3\text{mm}}$ with porous grains to that with compact grains, and derive a median value of 0.4. We observe a less than linear scaling relation between $F_{1.3\text{mm}}$ and M_{dust} . Such an outcome can be explained by two reasons. First, the higher optical depth with larger M_{dust} results in a stronger shielding of the inner disk regions, and therefore a lower mass-averaged dust temperature, see the comparison of $\tau_{\text{radial},0.55 \mu\text{m}} = 1$ surface between two models with different M_{dust} in Figure 3. Second, with the increasing M_{dust} , the millimeter optical depth increases as well, which will hide more disk interior regions and thus their reemitted flux, see the vertical optical depth at a wavelength of 1.3 mm in Figure 3. When the disk becomes optically thick, the millimeter emission gradually saturates. Therefore, the difference in $F_{1.3\text{mm}}$ decreases towards a higher M_{dust} .

The disk inner radius is fixed in the model grid. In this case, the disk outer radius defines the radial range in which dust grains are confined, and it significantly affects the optical depth and therefore the mass estimation. From the observational aspect, the disk outer radius is commonly characterized by the effective disk radius from spatially resolved images. Previous studies found a strong correlation between the effective disk radius and millimeter flux density (e.g., Tripathi et al. 2017; Andrews et al. 2018; Hendler et al. 2020). Using the 0.88 mm images, we compute the effective disk radius $R68$, i.e., the radius enclosing 68% of the total flux, to connect the statistics of our models to those obtained from observations in the literature. The results are presented in Figure 4. The effective disk radius depends mainly on the radial optical depth that is determined by the dust opacity and surface density (see Eq. 3). As can be seen in the upper panel, $R68$ increases with the characteristic radius R_c . Moreover, the range of $R68$ for each sampled R_c , indicated by the vertical length of the bars, is similar for models with the two types of grains. In the bottom panel of the figure, the blue curve and grey curve depict the boundaries within which the 7,920 models

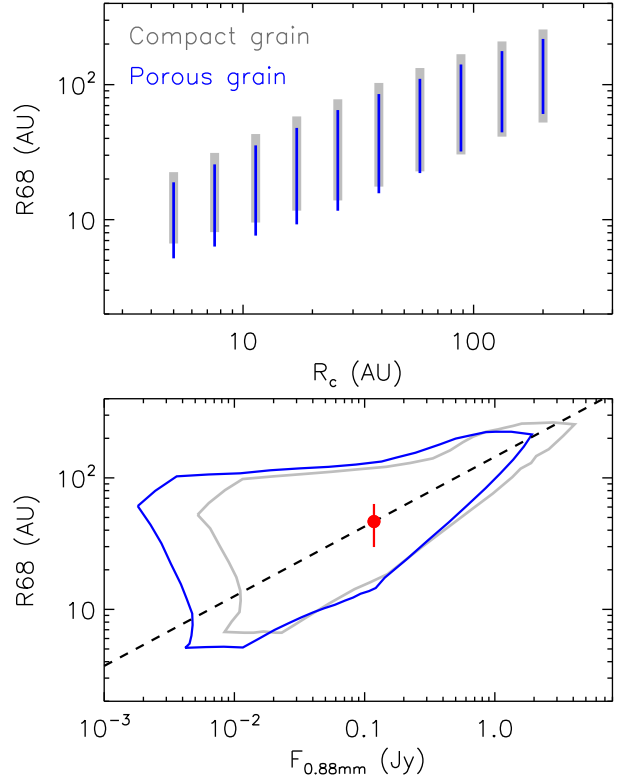


Fig. 4. Statistics of the effective disk radius $R68$ from the model grid. *Upper panel:* Ranges of $R68$ for each of the sampled R_c . The blue lines refer to the result when porous dust grains are considered, whereas the grey lines represent the case by using compact dust opacities. The thickness of lines is only for a better illustration. *Bottom panel:* Relation between $R68$ and $F_{0.88\text{mm}}$. The blue curve and grey curve enclose the regions occupied by the 9,360 models with porous grains and compact grains, respectively. The dashed line shows the relation $\log R68 = 2.16 + 0.53 \log F_{0.88\text{mm}}$ (Hendler et al. 2020). The red dot indicates the expected position of IRAS 04370+2559 in the diagram, see Sect. 4.2.

with porous dust opacities and compact dust opacities occupy in the $R68 - F_{0.88\text{mm}}$ diagram, respectively. Broadly, the blue curve is a shift of the grey curve towards the lower flux direction. Hendler et al. (2020) found that $R68$ correlates with $F_{0.88\text{mm}}$ via $\log R68 = 2.16 + 0.53 \log F_{0.88\text{mm}}$ for Taurus disks. Such a correlation, shown with the dashed line, is consistent with the trend revealed by our models.

3. Solid mass budget for planet formation

Based on self-consistent radiative transfer modeling, we have demonstrated that models with porous dust grains are systematically fainter in the millimeter, but the dust temperature is similar to that with compact grains. These facts have a consequence on the solid mass budget for planet formation. In this section, we calculate M_{dust} for a large sample of disks using Eq. 1, and compare the CDF of M_{dust} with that of exoplanet masses.

Manara et al. (2023) collected 0.88 mm and/or 1.3 mm flux densities for a large number of nearby disks. Assuming $\kappa_{\nu} = 2.3(\nu/230 \text{ GHz}) \text{ cm}^2/\text{g}$ and a constant $T_{\text{dust}} = 20$ K, they investigated the statistics of M_{dust} calculated with Eq. 1. In this work, we focus on the 718 disks with a similar age

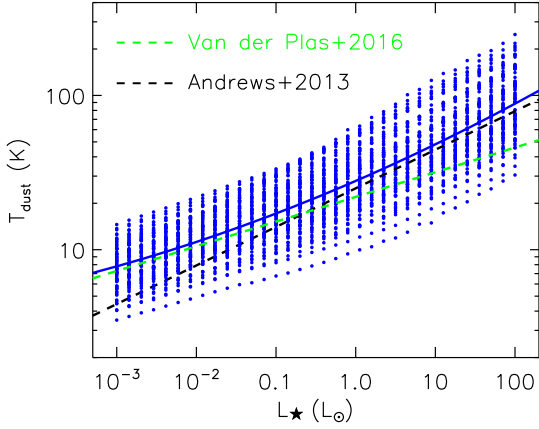


Fig. 5. Mass-averaged dust temperature as a function of stellar luminosity. The blue solid curve, expressed as $\log T_{\text{dust}} = 1.445 + 0.224 \log L_{\star} + 0.013 (\log L_{\star})^2$ is the best-fit relation to our models. The black dashed line refers to the relation $T_{\text{dust}} = 25 (L_{\star}/L_{\odot})^{0.25}$ K presented by Andrews et al. (2013). The green dashed line shows the relation $T_{\text{dust}} = 22 (L_{\star}/L_{\odot})^{0.16}$ K suggested by van der Plas et al. (2016).

(i.e., 1–3 Myr) in their sample, which are located in the Taurus, Lupus, Chamaeleon and Ophiuchus molecular clouds. The stellar luminosity of these sources spans a large range of $10^{-3} L_{\odot} \lesssim L_{\star} \lesssim 100 L_{\odot}$, therefore taking a constant T_{dust} is not appropriate. Andrews et al. (2013) showed that T_{dust} mainly depends on L_{\star} , and derived a relation $T_{\text{dust}} = 25 (L_{\star}/L_{\odot})^{0.25}$ K. Nevertheless, their results are based on radiative transfer models with a limited range of $0.1 L_{\odot} \lesssim L_{\star} \lesssim 100 L_{\odot}$. The scaling of T_{dust} with L_{\star} in the lower stellar mass regime was further investigated by van der Plas et al. (2016) and Hendl er et al. (2017), and the relation is found to be flatter $T_{\text{dust}} = 22 (L_{\star}/L_{\odot})^{0.16}$ K (van der Plas et al. 2016).

In order to homogenize our analysis, we re-calibrate the $T_{\text{dust}} - L_{\star}$ relation from massive young stars all the way down to the brown dwarf regime by creating a grid of radiative transfer models. The modeling framework is identical to that described in Section 2, and porous dust opacities are used in the simulation. We first sample 34 values of L_{\star} that are logarithmically distributed in the range of $[10^{-3} L_{\odot}, 100 L_{\odot}]$. Then, we interpolate the 2.5 Myr isochrone of pre-main-sequence evolutionary tracks to obtain T_{eff} and M_{\star} . For $L_{\star} < 0.4 L_{\odot}$ (approximately for $T_{\text{eff}} < 3900$ K), we adopt the models presented by Baraffe et al. (2015), whereas we take the nonmagnetic evolutionary models by Feiden (2016) for $L_{\star} \geq 0.4 L_{\odot}$. This procedure is motivated by the fact that the two sets of isochrones overlap well around $T_{\text{eff}} \sim 3900$ K. Once the stellar parameters are given, we use the corresponding BT-Sett1 models to represent the atmospheric spectra (Allard et al. 2011). In the grid, there are three points for Ψ : 1.05, 1.15, 1.25. We consider three values for h_{100} : 5 AU, 10 AU and 15 AU. For R_c , we also sample three values: 10 AU, 30 AU and 100 AU. We consider three disk-to-stellar mass ratios, i.e., 0.001, 0.01 and 0.1. Then, M_{dust} for each model is determined by assuming a gas-to-dust mass ratio of 100.

Figure 5 shows the mass-averaged dust temperature T_{dust} as a function of L_{\star} . Although there is a large dispersion in T_{dust} for each L_{\star} bin, an obvious trend is observed, with cooler disks around fainter stars. Moreover, the decreasing tendency of T_{dust} with L_{\star} appears steeper for stars with $L_{\star} \geq 0.2 L_{\odot}$ than that for systems with lower luminosities. The same phenomenon is also

seen in Figure 17 of Andrews et al. (2013), in which the dust temperature decrease seems to flatten out toward the low luminosity regime. We fit a polynomial (second order) to the correlation between T_{dust} and L_{\star} . The best fit is represented by

$$\log T_{\text{dust}} = 1.445 + 0.224 \log L_{\star} + 0.013 (\log L_{\star})^2. \quad (6)$$

Our relation for $L_{\star} < 0.2 L_{\odot}$ predicts similar dust temperature to the result given by van der Plas et al. (2016), whereas for $L_{\star} \geq 0.2 L_{\odot}$ we obtain similar dust temperature to the prescription of Andrews et al. (2013). The small difference between our and literature results is understood because of the difference in the choice of dust density distribution, disk parameters and dust opacities. For instance, we used porous dust opacities in the modeling, while other studies adopted compact dust opacities. Moreover, whether or not taking into account the stellar-mass dependent disk outer radius (Andrews et al. 2018; Andrews 2020) and interstellar radiation will also influence the heating of disks as a function of spectral type, and therefore affect the $T_{\text{dust}} - L_{\star}$ relation (e.g., van der Plas et al. 2016; Hendl er et al. 2017).

To calculate M_{dust} , we directly took L_{\star} , F_{ν} and D of each target provided by Manara et al. (2023). When L_{\star} is not available, we set $T_{\text{dust}} = 20$ K. The measured flux density at 1.3 mm is used with a higher priority since the optical depth is lower at longer wavelengths. The mass absorption coefficients of porous grains for the LGP are adopted in the calculation, i.e., $\kappa_{1.3\text{mm}} = 0.37 \text{ cm}^2/\text{g}$ and $\kappa_{0.88\text{mm}} = 0.84 \text{ cm}^2/\text{g}$. As can be seen in the upper panel of Figure 6, adopting porous dust opacities results in a systematically higher M_{dust} than that calculated by assuming $\kappa_{\nu} = 2.3(\nu/230 \text{ GHz}) \text{ cm}^2/\text{g}$ and a constant $T_{\text{dust}} = 20$ K. Moreover, we used the Kaplan-Meier estimator from the ASURV package to estimate the CDFs and median dust masses while properly accounting for the upper limits (Feigelson & Nelson 1985; Isobe et al. 1986). The median values are $1.6 M_{\oplus}$ and $9.3 M_{\oplus}$ for M_{dust} calculated by Manara et al. (2023) and in this study, respectively, which means that dust masses in protoplanetary disks may be underestimated by a factor of ~ 6 if the grains are in fact porous and not compact. For comparison, the grey curve in the bottom panel of Figure 6 shows the CDF of M_{dust} calculated with the porous dust opacities and a constant dust temperature $T_{\text{dust}} = 20$ K. The distribution is similar to that derived by scaling T_{dust} with L_{\star} . This is understood because the disks have a wide range of stellar luminosity $10^{-3} L_{\odot} \lesssim L_{\star} \lesssim 100 L_{\odot}$, and the effect of dust temperature on the distribution smooths out when the analysis is performed in a large sample scale. Mulders et al. (2021) analyzed the mass distribution of the exoplanet population detected from the Kepler transit survey (e.g., Borucki et al. 2010; Thompson et al. 2018) and radial velocity surveys from Mayor et al. (2011), because both surveys have a well-characterized detection bias. The red curve in the bottom panel of Figure 6 refers to the CDF of the exoplanet mass when accounting for observational selection and detection biases. The median mass of the exoplanets is $4.2 M_{\oplus}$ that is about two times lower than the median dust mass calculated in this work. Moreover, we do not see any exoplanetary systems with masses higher than the most massive disks. Our study shows that, if dust grains in disks are porous, the problem of insufficient mass for planet formation raised in the ALMA era may be resolved.

In the above analysis, we adopt an effective maximum grain size of 1 mm. The grain size has a direct impact on the dust opacity, and is commonly investigated via the millimeter spectral index (e.g., Andrews & Williams 2005; Ricci et al. 2010).

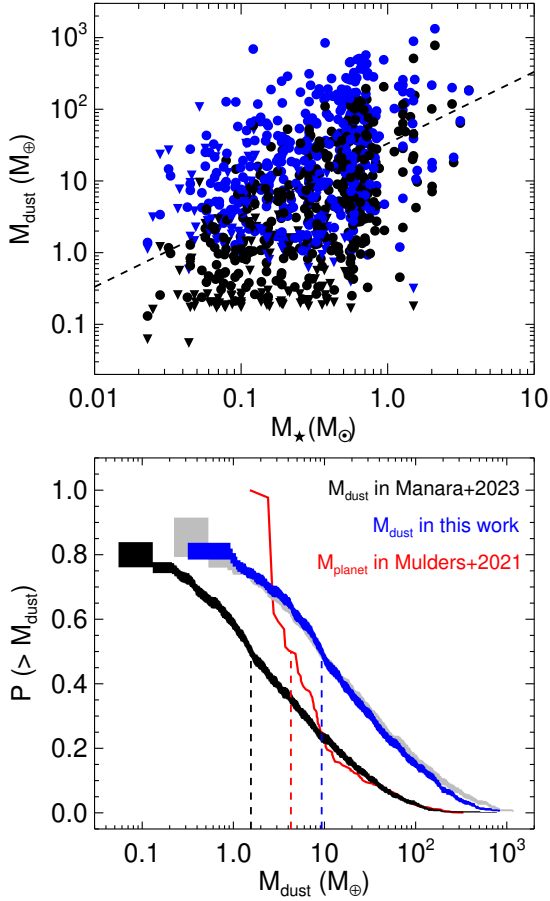


Fig. 6. Dust masses in protoplanetary disks and their statistics. *Upper panel:* M_{dust} as a function of M_{\star} . Black symbols show the results derived by Manara et al. (2023), while blue symbols represent our calculations considering porous dust opacities and a $T_{\text{dust}} - L_{\star}$ scaling given by Eq. 6, see Sect. 3. Millimeter detections are indicated with dots, whereas triangles mean upper limits of the millimeter flux are reported. The dashed line depicts the value of $100 \cdot M_{\text{dust}} = 0.01 \cdot M_{\star}$. *Bottom panel:* CDF of M_{dust} . The grey curve shows the result calculated with porous dust opacities and a constant dust temperature $T_{\text{dust}} = 20$ K. The red curve refers to the distribution of exoplanet masses obtained by Mulders et al. (2021). The vertical dashed lines mark the median values of each distribution.

Future observations at multiple (sub-)millimeter wavelengths are needed to constrain the grain size that is essential for a better characterization of the dust mass distribution. To observationally prove that dust grains are porous and constrain the porosity \mathcal{P} , multiwavelength observations and analysis are mandatory.

Grain porosity alters the absorption, scattering and polarization behavior of dust grains (e.g., Semenov et al. 2003; Ysard et al. 2018), and therefore influences the observable appearance of protoplanetary disks. The position, strengths, width, and shape of dust emission features in the mid-infrared domain depend on the grain structure (e.g., Voshchinnikov & Henning 2008; Vaidya & Gupta 2011). Detailed decomposition of spectra obtained with the Infrared Spectrograph (IRS) on board Spitzer has demonstrated that the emission bands of forsterite and enstatite are best matched with porous grains, rather than compact spherical grains (e.g., Bouwman et al. 2008; Juhász et al. 2010). Analyzing the spectra from the Mid-Infrared Instrument (MIRI)

equipped on JWST gives the same conclusion (e.g., Jang et al. 2024). The accumulating MIRI spectra will shed more insights into the dust properties particularly in faint disks that were not accessible by Spitzer.

Kirchschlager & Wolf (2014) found that grain porosity strongly influences the scattered-light maps of protoplanetary disks. For highly tilted disks (e.g., $i \geq 75^\circ$), the flux of the scattered light at optical wavelengths is significantly enlarged when porous dust opacities are included. Once the disk deviates from a face-on orientation (e.g., $i \geq 5^\circ$), the scattered light maps show a dark lane that is characteristic for inclined disks. The dark lane appears more pronounced assuming compact dust opacities. By analyzing scattered-light maps from radiative transfer simulations, Tazaki et al. (2019b) found that porous dust aggregates large compared to near-infrared wavelengths show marginally grey or slightly blue in total or polarized intensity, while large compact dust grains give rise to reddish scattered-light colours in total intensity. High resolution near-infrared observations can be used to verify the model predictions (e.g., Fukagawa et al. 2010; Avenhaus et al. 2018).

There exist significant differences between polarimetric images of disks composed of porous particles and compact spheres (Min et al. 2012). Simulated polarization maps at optical wavelengths reveal an increase in the polarization degree by a factor of about four when porous grains are considered (Kirchschlager & Wolf 2014). The wavelength dependent polarization reversal (i.e., 90° flip of the polarization direction at visible light) depends strongly on the grain porosity, and thus has diagnostic potential for dust properties. Tazaki et al. (2019a) investigated how the grain structure and porosity alter polarimetric images at millimeter wavelengths. The polarization pattern of disks containing moderately porous particles show near- and far-side asymmetries at (sub-)millimeter wavelengths. Porous grains exhibit a weaker wavelength dependence of scattering polarization than solid spherical grains. Brunngräber & Wolf (2021) investigated the effect of grain porosity on the polarization degree due to self-scattering in the (sub-)millimeter wavelength range. They found that porous dust grains with moderate filling factors of about 10% increase the degree of polarization by up to a factor of four compared to compact grains. However, the degree of polarization drops rapidly when the porosity is very high, with a filling factor of 1% or lower, because of the low opacity and optical depth. These theoretical studies show that multi-wavelength polarimetric observations are crucial to constrain the structure and porosity of dust grains in protoplanetary disks (e.g., Zhang et al. 2023; Ueda et al. 2024).

4. Modeling the SED of IRAS 04370+2559

Protoplanetary disks, especially in the inner region and dense midplane, are likely to be optically thick at millimeter wavelengths (e.g., Wolf et al. 2008; Pinte et al. 2016; Liu et al. 2019; Ueda et al. 2020), which means that M_{dust} estimated using Eq. 1 is underestimated. Therefore, in reality the CDF of M_{dust} should shift towards the higher abscissa value in Figure 6. Self-consistent radiative transfer modeling is an appropriate way to treat the optical depth effect, and therefore better constrain the dust mass. In this section, we conduct a detailed modeling for the SED of the IRAS 04370+2559 disk, and showcase the difference in M_{dust} derived using different approaches and dust opacities.

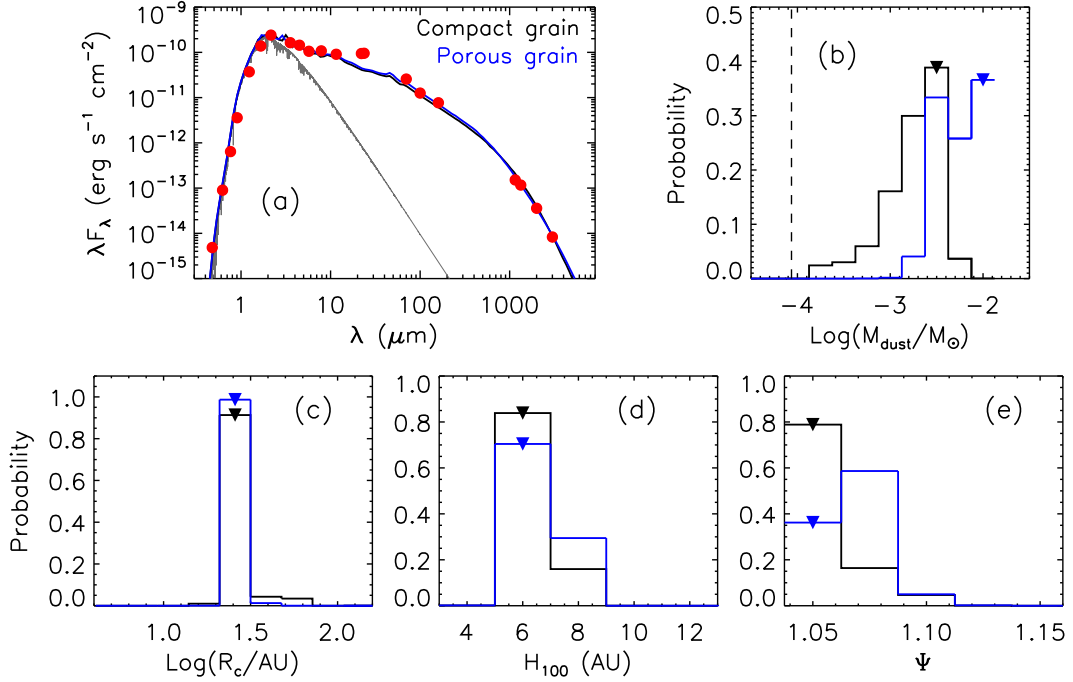


Fig. 7. Fitting results of the IRAS 04370+2559 disk. *Panel (a)*: SEDs of IRAS 04370+2559. The best-fit radiative transfer models with compact dust opacities and porous dust opacities are shown with black lines and blue lines, respectively. The grey curve refers to the input BT-Settl spectrum, and photometric data points are overlaid with red dots. *Panels (b)–(e)*: Bayesian probability distributions for $\text{Log}_{10}(M_{\text{dust}}/M_{\odot})$, $\text{Log}_{10}(R_{\text{c}}/\text{AU})$, H_{100} and Ψ . The triangles indicate the best-fit parameter values. The vertical dashed line in panel (b) marks the analytic dust mass calculated with Eq. 1 by assuming $T_{\text{dust}} = 20$ K and $\kappa_{1.3\text{mm}} = 2.3$ cm²/g.

4.1. Build the observed SED with new IRAM/NIKA-2 observations

IRAS 04370+2559 is a T Tauri star located in the Taurus star formation region at a distance of $D = 137.4$ pc (Gaia Collaboration et al. 2023). Besides the stellar properties of IRAS 04370+2559 is representative for T Tauri stars (Gullbring et al. 1998), there are two reasons why we select it for the test. First, a large number of photometric data points from optical to millimeter regimes are available either in the archive or from our new IRAM/NIKA-2 observations. Second, the observed SED of IRAS 04370+2559, shown with red dots in panel (a) of Figure 7, displays a flux drop at $\lambda \sim 70$ μm . This is a strong indication of dust settling (Liu et al. 2012; Dullemond & Dominik 2004; D’Alessio et al. 2006), which implies that a huge amount of material is very likely concentrated close to the disk midplane, creating high optical depths. In this case, a detailed modeling of the SED is necessary to constrain the dust mass, and it is expected to have a large difference in M_{dust} derived with different approaches. To compile the SED, we collect photometry from the Sloan Digital Sky Survey (Adelman-McCarthy et al. 2011), 2MASS catalog (Skrutskie et al. 2006), Spitzer/IRAC and MIPS measurements (Luhman et al. 2010; Rebull et al. 2010) and Herschel/PACS data (Ribas et al. 2017). In the millimeter, there are data points at 1.3 mm and 3 mm obtained with the Submillimeter Array (Andrews et al. 2013) and Combined Array for Research in Millimeter-wave Astronomy (Babaian 2020), respectively.

We conduct new IRAM/NIKA-2 observations towards the IRAS 04370+2559 disk. Details about the observation, data reduction and flux extraction are described in Appendix A. The measured flux densities at 1.1 mm and 2 mm are 58.2 ± 2.4 mJy and 23.9 ± 0.6 mJy, respectively. These efforts allow us to build the SED with an excellent wavelength coverage, see panel (a) of

Figure 7. Andrews et al. (2013) fitted the optical part of the SED, and derived $T_{\text{eff}} = 3778$ K and $L_{\star} = 0.9 L_{\odot}$ assuming a distance of 140 pc. We rescale their stellar luminosity by adopting the Gaia distance of $D = 137.4$ pc (Gaia Collaboration et al. 2023), yielding $L_{\star} = 0.86 L_{\odot}$. Moreover, an extinction of $A_V = 10.65$ mag is required to reproduce the optical photometry. We use the extinction law of Cardelli et al. (1989) with $R_V = 3.1$.

4.2. Results

Using the model grid generated in Sect. 2, we evaluate the quality of fit to the SED by using the χ^2_{SED} metric. We also compare the expected effective disk radius $R68_{\text{exp}}$ of IRAS 04370+2559 with the $R68$ value of each model, because the disk size has an important influence on the derived dust mass (Ballering & Eisner 2019; Liu et al. 2022). First, an expected 0.88 mm flux is derived by extrapolating the millimeter part of the observed SED. Then, we calculate $R68_{\text{exp}}$ using the Hendler et al. (2020) relation

$$\log R68 = (2.16 \pm 0.11) + (0.53 \pm 0.12) \log F_{0.88\text{mm}}. \quad (7)$$

The derived $R68_{\text{exp}} = 46.6 \pm 16.7$ AU is shown with the red dot in the bottom panel of Figure 4. A comparison of $R68$ between the observation and model predictions gives an extra term to the total fit metric

$$\chi^2 = \chi^2_{\text{SED}} + g \chi^2_{R68}. \quad (8)$$

The g factor is used to balance the weighting between both observables, and it is determined by comparing the median χ^2_{SED} with median χ^2_{R68} of all the models.

We conduct a Bayesian analysis by assuming flat priors for each parameter. The relative probability of a model in the parameter space is given by $\exp(-\chi^2/2)$ (e.g., Lay et al. 1997; Pinte

et al. 2008). Then, the marginalized probability distribution for each parameter is obtained by first adding the individual probabilities of all the models with a common value of the parameter, and then normalizing to the total probability for that parameter. The resulting marginalized probability distributions are presented in panels (b)–(e) of Figure 7. The triangles indicate the parameter values of the best-fit model, most of which are identical to the most probable values.

The best-fit model with porous dust opacities have a dust mass of $0.01 M_{\odot}$ that is about 3 times larger than the best-fit value $3.2 \times 10^{-3} M_{\odot}$ when including compact dust opacities. To calculate the analytic dust mass using Eq. 1, we adopt $\kappa_{1.3\text{mm}} = 2.3 \text{ cm}^2/\text{g}$ and $T_{\text{dust}} = 20 \text{ K}$ for consistency with literature works. We take $F_{1.3\text{mm}} = 51.7 \text{ mJy}$ (Andrews et al. 2013), and derive $M_{\text{dust,ana}} = 8.6 \times 10^{-5} M_{\odot}$, which is indicated with the vertical dashed line in panel (b) of Figure 7. The dust masses from radiative transfer modeling with porous grains and compact grains are 116 and 37 times higher than the analytic dust mass, respectively. In order to disentangle the effects of dust porosity and running radiative transfer modeling on the difference in the mass determination, we further calculate the analytic dust mass using $\kappa_{1.3\text{mm}} = 0.37 \text{ cm}^2/\text{g}$ of porous grains for the LGP. The derived mass $5.4 \times 10^{-4} M_{\odot}$ is about 6 times higher than that calculated with $\kappa_{1.3\text{mm}} = 2.3 \text{ cm}^2/\text{g}$. Comparing this factor with 116 indicates that running radiative transfer models is mostly responsible for the large difference. We note that whether dust porosity or radiative transfer modeling contributes more to the difference in the mass determination varies from source to source, as previous studies show that the factor of mass underestimation induced by radiative transfer modeling ranges from a few to hundreds depending on the optical depth of the disk (Ballering & Eisner 2019; Liu et al. 2022).

The significant difference in M_{dust} between the traditionally analytic calculation and radiative transfer modeling is due to two main reasons. First, the best-fit model features a low flaring index ($\Psi = 1.05$) and scale height ($h_{100} = 6 \text{ AU}$), leading to a low mass-averaged dust temperature $T_{\text{dust}} \sim 14 \text{ K}$. Second, a small characteristic radius $R_c = 25.8 \text{ AU}$ is required to reproduce the expected effective radius $R_{68\text{exp}}$. The narrow radial density distribution creates highly optically thick regions, resulting in a large underestimation of M_{dust} . We further use the 3 mm flux $F_{3\text{mm}} = 8.3 \text{ mJy}$ (Babaian 2020) and $\kappa_{\nu} = 2.3(\nu/230 \text{ GHz}) \text{ cm}^2/\text{g}$ to calculate the analytic dust mass. The result is $M_{\text{dust,ana}} = 1.4 \times 10^{-4} M_{\odot}$, roughly 2 times larger than that derived with the 1.3 mm data. This implies that the IRAS 04370+2559 disk is likely optically thick at 1.3 mm. Future spatially resolved observations at longer wavelengths are required to constrain the disk size and dust density distribution that allow a better measurement of the dust mass (e.g., Macías et al. 2021; Guidi et al. 2022; Guerra-Alvarado et al. 2024).

5. Summary

The total dust mass in protoplanetary disks is an important parameter that evaluates the potential for planet formation. The determination of dust mass is dependent on the choice of dust properties. There is growing evidence that dust grains in protoplanetary disks might be porous. In this work, using self-consistent radiative transfer models, we compared the dust temperature T_{dust} and emergent millimeter fluxes between models incorporating compact dust opacities and porous dust opacities.

The results show that T_{dust} is similar between models with the two types of dust opacities, but porous dust grains yield systematically lower millimeter fluxes than compact dust grains be-

cause of the lower emissivity. This fact has a pronounced impact on the solid mass budget for planet formation. We re-calibrated the $T_{\text{dust}} - L_{\star}$ relation for a wide range of stellar mass, and obtained a second-order polynomial in the explored stellar mass regime. We calculated the analytic dust masses of a large sample of disks with our $T_{\text{dust}} - L_{\star}$ relation and porous dust opacities. The median dust mass $9.3 M_{\oplus}$ is about 6 times higher than the literature result $1.6 M_{\oplus}$, and it is about 2 times higher than the median mass of exoplanets investigated by Mulders et al. (2021). A comparison of the CDF between disk dust masses and exoplanet masses shows that there are no exoplanetary systems with masses higher than the most massive disks, if dust grains in disks are in fact porous. Our study suggests that adopting porous dust opacities may alleviate the problem of insufficient dust solids for planet formation.

Mass calculation using the traditionally analytic approach always underestimates the true value due to the optical depth effect. We took the IRAS 04370+2559 disk as an example to show a combined effect of optical depth and porous dust opacities on the mass estimation. We conducted new IRAM/NIKA-2 observations towards IRAS 04370+2559, enabling a better wavelength sampling of the observed SED. A large grid of radiative transfer models are fitted to the observation. The best-fit dust mass is about 100 times larger than the analytic dust mass when the porous dust opacities are adopted in the modeling.

Acknowledgements. We thank the anonymous referee for the constructive comments that highly improved the manuscript. YL acknowledges financial supports by the Natural Science Foundation of China (Grant No. 11973090), and by the International Partnership Program of Chinese Academy of Sciences (Grant number 019GJHZ2023016FN). This work is based on observations carried out under project number 040-17 with the IRAM 30m telescope. IRAM is supported by INSU/CNRS (France), MPG (Germany) and IGN (Spain). We would like to thank the IRAM staff for their support during the NIKA2 campaigns. The NIKA2 dilution cryostat has been designed and built at the Institut Néel. We acknowledge the crucial contribution of the Cryogenics Group, and in particular Gregory Garde, Henri Rodenas, Jean Paul Leggeri, Philippe Camus. This work has been partially funded by the Foundation Nanoscience Grenoble and the LabEx FOCUS ANR-11-LABX-0013 and is supported by the French National Research Agency under the contracts “MKIDS”, “NIKA” and ANR-15-CE31-0017 and in the framework of the “Investissements d’avenir” program (ANR-15-IDEX-02). This work has benefited from the support of the European Research Council Advanced Grant ORISTARS under the European Union’s Seventh Framework Programme (Grant Agreement no. 291294). The NIKA2 data were pre-processed and calibrated with the NIKA2 collaboration pipeline. This research has made use of Herschel data; Herschel is an ESA space observatory with science instruments provided by European-led Principal Investigator consortia and with important participation from NASA. FK has received funding from the European Research Council (ERC) under the European Union’s Horizon 2020 research and innovation programme DustOrigin (ERC-2019-StG-851622). In this study, a cluster is used with the SIMT accelerator made in China. The cluster includes many nodes each containing 4 CPUs and 8 accelerators. The accelerator adopts a GPU-like architecture consisting of a 16GB HBM2 device memory and many compute units. Accelerators connected to CPUs with PCI-E, the peak bandwidth of the data transcription between main memory and device memory is 16GB/s. This work is partially supported by cosmology simulation database (CSD) in the National Basic Science Data Center (NBSDC-DB-10).

References

- Adelman-McCarthy, J. K. & et al. 2011, VizieR Online Data Catalog: The SDSS Photometric Catalog, Release 8 (Adelman-McCarthy+, 2011), VizieR Online Data Catalog: II/306. Originally published in: To be published
- Allard, F., Homeier, D., & Freytag, B. 2011, in Astronomical Society of the Pacific Conference Series, Vol. 448, 16th Cambridge Workshop on Cool Stars, Stellar Systems, and the Sun, ed. C. Johns-Krull, M. K. Browning, & A. A. West, 91
- Andrews, S. M. 2020, ARA&A, 58, 483
- Andrews, S. M., Rosenfeld, K. A., Kraus, A. L., & Wilner, D. J. 2013, ApJ, 771, 129
- Andrews, S. M., Terrell, M., Tripathi, A., et al. 2018, ApJ, 865, 157
- Andrews, S. M. & Williams, J. P. 2005, ApJ, 631, 1134

- Andrews, S. M., Wilner, D. J., Espaillat, C., et al. 2011, *ApJ*, 732, 42
- Ansdell, M., Williams, J. P., van der Marel, N., et al. 2016, *ApJ*, 828, 46
- Avenhaus, H., Quanz, S. P., Garufi, A., et al. 2018, *ApJ*, 863, 44
- Babaian, D. 2020, A survey of protoplanetary disks in the Taurus star forming region at millimeter wavelengths, Master Thesis, California State University, Northridge
- Ballering, N. P. & Eisner, J. A. 2019, *AJ*, 157, 144
- Baraffe, I., Homeier, D., Allard, F., & Chabrier, G. 2015, *A&A*, 577, A42
- Barenfeld, S. A., Carpenter, J. M., Ricci, L., & Isella, A. 2016, *ApJ*, 827, 142
- Birnstiel, T. 2023, arXiv e-prints, arXiv:2312.13287
- Birnstiel, T., Dullemond, C. P., Zhu, Z., et al. 2018, *ApJ*, 869, L45
- Borucki, W. J., Koch, D., Basri, G., et al. 2010, *Science*, 327, 977
- Bouwman, J., Henning, T., Hillenbrand, L. A., et al. 2008, *ApJ*, 683, 479
- Bruggeman, D. 1935, *Ann. Phys.*, 416, 636
- Brunngräber, R. & Wolf, S. 2021, *A&A*, 648, A87
- Cardelli, J. A., Clayton, G. C., & Mathis, J. S. 1989, *ApJ*, 345, 245
- Cazzoletti, P., Manara, C. F., Liu, H. B., et al. 2019, *A&A*, 626, A11
- D'Alessio, P., Calvet, N., Hartmann, L., Franco-Hernández, R., & Servín, H. 2006, *ApJ*, 638, 314
- Dominik, C., Min, M., & Tazaki, R. 2021, OpTool: Command-line driven tool for creating complex dust opacities, *Astrophysics Source Code Library*, record ascl:2104.010
- Dominik, C. & Tielens, A. G. G. M. 1997, *ApJ*, 480, 647
- Draine, B. T. 2003, *ARA&A*, 41, 241
- Draine, B. T. & Flatau, P. J. 1994, *Journal of the Optical Society of America A*, 11, 1491
- Draine, B. T. & Flatau, P. J. 2010, arXiv e-prints, arXiv:1002.1505
- Dullemond, C. P. & Dominik, C. 2004, *A&A*, 421, 1075
- Dullemond, C. P., Juhasz, A., Pohl, A., et al. 2012, RADMC-3D: A multi-purpose radiative transfer tool, *Astrophysics Source Code Library*
- Eistrup, C. & Henning, T. 2022, *A&A*, 667, A160
- Ejlali, G., Adam, R., Ade, P., et al. 2024, in *European Physical Journal Web of Conferences*, Vol. 293, *European Physical Journal Web of Conferences*, 00016
- Feiden, G. A. 2016, *A&A*, 593, A99
- Feigelson, E. D. & Nelson, P. I. 1985, *ApJ*, 293, 192
- Fukagawa, M., Tamura, M., Itoh, Y., et al. 2010, *PASJ*, 62, 347
- Gaia Collaboration, Vallenari, A., Brown, A. G. A., et al. 2023, *A&A*, 674, A1
- Garrod, R. T. & Herbst, E. 2006, *A&A*, 457, 927
- Ginski, C., Tazaki, R., Dominik, C., & Stolker, T. 2023, *ApJ*, 953, 92
- Grant, S. L., Espaillat, C. C., Wendeborn, J., et al. 2021, *ApJ*, 913, 123
- Guerra-Alvarado, O. M., Carrasco-González, C., Macías, E., et al. 2024, *A&A*, 686, A298
- Guidi, G., Isella, A., Testi, L., et al. 2022, *A&A*, 664, A137
- Gullbring, E., Hartmann, L., Briceño, C., & Calvet, N. 1998, *ApJ*, 492, 323
- Gupta, A., Miotello, A., Manara, C. F., et al. 2023, *A&A*, 670, L8
- Gupta, A., Miotello, A., Williams, J. P., et al. 2024, *A&A*, 683, A133
- Harsono, D., Bruderer, S., & van Dishoeck, E. F. 2015, *A&A*, 582, A41
- Hartmann, L. 2009, *Accretion Processes in Star Formation: Second Edition*
- Hendler, N., Pascucci, I., Pinilla, P., et al. 2020, *ApJ*, 895, 126
- Hendler, N. P., Mulders, G. D., Pascucci, I., et al. 2017, *ApJ*, 841, 116
- Henning, T. & Semenov, D. 2013, *Chemical Reviews*, 113, 9016
- Henning, T. & Stognienko, R. 1996, *A&A*, 311, 291
- Hsieh, C.-H., Arce, H. G., José Maureira, M., et al. 2024, arXiv e-prints, arXiv:2404.02809
- Isobe, T., Feigelson, E. D., & Nelson, P. I. 1986, *ApJ*, 306, 490
- Jang, H., Waters, R., Kaeufer, T., et al. 2024, arXiv e-prints, arXiv:2408.16367
- Jorda, L., Gaskell, R., Capanna, C., et al. 2016, *Icarus*, 277, 257
- Juhász, A., Bouwman, J., Henning, T., et al. 2010, *ApJ*, 721, 431
- Kataoka, A., Tanaka, H., Okuzumi, S., & Wada, K. 2013, *A&A*, 557, L4
- Kirchschlager, F., Bertrang, G. H. M., & Flock, M. 2019, *MNRAS*, 488, 1211
- Kirchschlager, F. & Wolf, S. 2013, *A&A*, 552, A54
- Kirchschlager, F. & Wolf, S. 2014, *A&A*, 568, A103
- Kirchschlager, F., Wolf, S., & Madlener, D. 2016, *MNRAS*, 462, 858
- Kley, W. & Nelson, R. P. 2012, *ARA&A*, 50, 211
- Kofman, W., Herique, A., Barbin, Y., et al. 2015, *Science*, 349, 2.639
- Krijt, S., Ciesla, F. J., & Bergin, E. A. 2016, *ApJ*, 833, 285
- Lay, O. P., Carlstrom, J. E., & Hills, R. E. 1997, *ApJ*, 489, 917
- Liu, H. B. 2019, *ApJ*, 877, L22
- Liu, Y., Dipierro, G., Ragusa, E., et al. 2019, *A&A*, 622, A75
- Liu, Y., Henning, T., Carrasco-González, C., et al. 2017, *A&A*, 607, A74
- Liu, Y., Linz, H., Fang, M., et al. 2022, *A&A*, 668, A175
- Liu, Y., Madlener, D., Wolf, S., Wang, H., & Ruge, J. P. 2012, *A&A*, 546, A7
- Luhman, K. L., Allen, P. R., Espaillat, C., Hartmann, L., & Calvet, N. 2010, *ApJS*, 186, 111
- Lynden-Bell, D. & Pringle, J. E. 1974, *MNRAS*, 168, 603
- Macías, E., Guerra-Alvarado, O., Carrasco-González, C., et al. 2021, *A&A*, 648, A33
- Manara, C. F., Ansdell, M., Rosotti, G. P., et al. 2023, in *Astronomical Society of the Pacific Conference Series*, Vol. 534, *Protostars and Planets VII*, ed. S. Inutsuka, Y. Aikawa, T. Muto, K. Tomida, & M. Tamura, 539
- Manara, C. F., Morbidelli, A., & Guillot, T. 2018, *A&A*, 618, L3
- Mayor, M., Marmier, M., Lovis, C., et al. 2011, arXiv e-prints, arXiv:1109.2497
- Michoulier, S., Gonzalez, J.-F., & Price, D. J. 2024, *A&A*, 688, A31
- Min, M., Canovas, H., Mulders, G. D., & Keller, C. U. 2012, *A&A*, 537, A75
- Miotello, A., Kamp, I., Birnstiel, T., Cleeves, L. C., & Kataoka, A. 2023, in *Astronomical Society of the Pacific Conference Series*, Vol. 534, *Protostars and Planets VII*, ed. S. Inutsuka, Y. Aikawa, T. Muto, K. Tomida, & M. Tamura, 501
- Mulders, G. D., Pascucci, I., Ciesla, F. J., & Fernandes, R. B. 2021, *ApJ*, 920, 66
- Natta, A., Testi, L., Calvet, N., et al. 2007, in *Protostars and Planets V*, ed. B. Reipurth, D. Jewitt, & K. Keil, 767
- Öberg, K. I., Facchini, S., & Anderson, D. E. 2023, *ARA&A*, 61, 287
- Ohashi, N., Tobin, J. J., Jørgensen, J. K., et al. 2023, *ApJ*, 951, 8
- Okuzumi, S., Tanaka, H., Kobayashi, H., & Wada, K. 2012, *ApJ*, 752, 106
- Paardekooper, S., Dong, R., Duffell, P., et al. 2023, in *Astronomical Society of the Pacific Conference Series*, Vol. 534, *Protostars and Planets VII*, ed. S. Inutsuka, Y. Aikawa, T. Muto, K. Tomida, & M. Tamura, 685
- Pascucci, I., Testi, L., Herczeg, G. J., et al. 2016, *ApJ*, 831, 125
- Perotto, L., Ponthieu, N., Macías-Pérez, J. F., et al. 2020, *A&A*, 637, A71
- Pinte, C., Dent, W. R. F., Ménard, F., et al. 2016, *ApJ*, 816, 25
- Pinte, C., Padgett, D. L., Ménard, F., et al. 2008, *A&A*, 489, 633
- Purcell, E. M. & Pennypacker, C. R. 1973, *ApJ*, 186, 705
- Rebull, L. M., Padgett, D. L., McCabe, C. E., et al. 2010, *ApJS*, 186, 259
- Ribas, Á., Espaillat, C. C., Macías, E., et al. 2017, *ApJ*, 849, 63
- Ricci, L., Testi, L., Natta, A., & Brooks, K. J. 2010, *A&A*, 521, A66
- Rilinger, A. M., Espaillat, C. C., Xin, Z., et al. 2023, *ApJ*, 944, 66
- Roussel, H. 2013, *PASP*, 125, 1126
- Savvidou, S. & Bitsch, B. 2024, arXiv e-prints, arXiv:2407.08533
- Schwarz, K. R., Calahan, J. K., Zhang, K., et al. 2021, *ApJS*, 257, 20
- Segura-Cox, D. M., Schmiedeke, A., Pineda, J. E., et al. 2020, *Nature*, 586, 228
- Semenov, D., Henning, T., Helling, C., Ilgner, M., & Sedlmayr, E. 2003, *A&A*, 410, 611
- Sheehan, P. D., Tobin, J. J., Federman, S., Megeath, S. T., & Looney, L. W. 2020, *ApJ*, 902, 141
- Sierra, A. & Lizano, S. 2020, *ApJ*, 892, 136
- Skrutskie, M. F., Cutri, R. M., Stiening, R., et al. 2006, *AJ*, 131, 1163
- Stammler, S. M., Birnstiel, T., Panić, O., Dullemond, C. P., & Dominik, C. 2017, *A&A*, 600, A140
- Stognienko, R., Henning, T., & Ossenkopf, V. 1995, *A&A*, 296, 797
- Stolker, T., Dominik, C., Avenhaus, H., et al. 2016, *A&A*, 595, A113
- Tazaki, R., C., & Dominik, C. 2023, *ApJ*, 944, L43
- Tazaki, R., Tanaka, H., Kataoka, A., Okuzumi, S., & Muto, T. 2019a, *ApJ*, 885, 52
- Tazaki, R., Tanaka, H., Muto, T., Kataoka, A., & Okuzumi, S. 2019b, *MNRAS*, 485, 4951
- Tazzari, M., Testi, L., Natta, A., et al. 2021, *MNRAS*, 506, 5117
- Thompson, S. E., Coughlin, J. L., Hoffman, K., et al. 2018, *ApJS*, 235, 38
- Tripathi, A., Andrews, S. M., Birnstiel, T., & Wilner, D. J. 2017, *ApJ*, 845, 44
- Tychoniec, Ł., Manara, C. F., Rosotti, G. P., et al. 2020, *A&A*, 640, A19
- Tychoniec, Ł., Tobin, J. J., Karska, A., et al. 2018, *ApJS*, 238, 19
- Ueda, T., Kataoka, A., & Tsukagoshi, T. 2020, *ApJ*, 893, 125
- Ueda, T., Tazaki, R., Okuzumi, S., Flock, M., & Sudarshan, P. 2024, *Nature Astronomy*
- Vaidya, D. B. & Gupta, R. 2011, *A&A*, 528, A57
- van der Marel, N., Williams, J. P., Ansdell, M., et al. 2018, *ApJ*, 854, 177
- van der Plas, G., Ménard, F., Ward-Duong, K., et al. 2016, *ApJ*, 819, 102
- Voshchinnikov, N. V. & Henning, T. 2008, *A&A*, 483, L9
- Warren, S. G. & Brandt, R. E. 2008, *Journal of Geophysical Research (Atmospheres)*, 113, D14220
- Williams, J. P. & Cieza, L. A. 2011, *ARA&A*, 49, 67
- Wolf, S., Schegerer, A., Beuther, H., Padgett, D. L., & Stapelfeldt, K. R. 2008, *ApJ*, 674, L101
- Wurm, G. & Blum, J. 1998, *Icarus*, 132, 125
- Xin, Z., Espaillat, C. C., Rilinger, A. M., Ribas, Á., & Macías, E. 2023, *ApJ*, 942, 4
- Ysard, N., Jones, A. P., Demyk, K., Boutéraon, T., & Koehler, M. 2018, *A&A*, 617, A124
- Zhang, K., Booth, A. S., Law, C. J., et al. 2021, *ApJS*, 257, 5
- Zhang, S., Zhu, Z., Ueda, T., et al. 2023, *ApJ*, 953, 96
- Zhu, Z., Zhang, S., Jiang, Y.-F., et al. 2019, *ApJ*, 877, L18

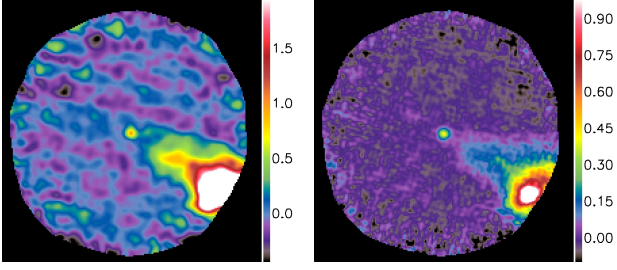


Fig. A.1. NIKA2 maps of IRAS 04370+2559 at 1.1 mm (left) and 2.0 mm (right) in mJy/pixel. The pixel size is $3''$ and the data have been convolved to a FWHM resolution of $20''$.

Appendix A: IRAM/NIKA-2 observations of the IRAS 04370+2559 disk

In this section, we present the details about the observations and data reduction of the IRAM/NIKA-2 observations towards IRAS 04370+2559. The on-the-fly observations were conducted simultaneously at 1.25 and 2 mm as part of the IRAM project 040-17 on October 27, 2017 in four consecutive scans, for a total duration of 8.9 min. The mean elevation of the source was 73° and the mean opacity at this elevation was on the order of 0.13 at 2 mm and 0.32 at 1.25 mm. The sky rms was low and stable.

The data were processed with the *Scanam.nika* package, a branch of *Scanamorphos* adapted to NIKA-2 data (Roussel 2013). The underlying principle is the same as for Herschel data, i.e. the full exploitation of the redundancy built in the observations to subtract the atmospheric and instrumental noise from the data. More details are given in Ejlali et al. (2024). The flux calibration established by Perotto et al. (2020) is refined based on aperture photometry on more than a hundred finely-sampled maps of Uranus observed from October 2017 to January 2023. This leads to beam solid angles of (188 ± 11) and (381 ± 11) square arcseconds at 1.15 and 2 mm, respectively.

The maps are shown in Figure A.1. To assess the reliability of the photometry, simulations were performed, using as input the longest-wavelength infrared data shortward of 1.15 mm where the source is detected, i.e. the PACS $160\ \mu\text{m}$ map. Time series were simulated from this map as if they had been obtained with NIKA-2, with the same observation geometry and sampling. They were rescaled so that the median signal-to-noise ratio for the source was identical in the simulation and in the NIKA-2 observations. The noise extracted from NIKA-2 data was added, and then the resulting time series were processed in the same fashion as the real data, and the final map was rescaled back to the original unit. The results for the 2 mm noise are shown in Figure A.2. They confirm that while the recovery of extended emission is challenging in such small and shallow maps, the source of interest is preserved, since no residual is visible at its location in the difference map between the simulation input and output.

Photometric information from the NIKA2 maps was gathered via aperture photometry. We used an aperture radius of $15''$ and subtracted a local background estimated in an annulus between $30 - 50''$, avoiding the extended emission associated with the bright source to the south-west (i.e., L 1527 IRS). We corrected these fluxes by aperture correction factors estimated from the above-mentioned Uranus observations. We arrive at the following flux densities:

$$F_\nu(1.1\text{ mm}) = 58.2\text{ mJy} \pm 2.4\text{ mJy} \pm 3.5\text{ mJy},$$

$$F_\nu(2.0\text{ mm}) = 23.9\text{ mJy} \pm 0.6\text{ mJy} \pm 0.8\text{ mJy}.$$

The first error term is derived from the random noise in the pho-

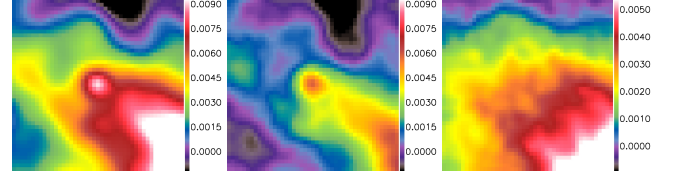


Fig. A.2. Simulation of the effect of the 2 mm noise on the data: zoom on the input $160\text{-}\mu\text{m}$ map (left), on the simulation output (middle) and on the difference between the two maps, with a smaller dynamic range (right). The pixel size and FWHM resolution are the same as in Figure A.1, and the flux unit is Jy/pixel.

tometry aperture via $\sigma_{(\text{flux density})} = \sqrt{N_{\text{pix}}} \times \sigma_{\text{map}}$, with N_{pix} denoting the number of pixels in the aperture. The second term assumes formal uncertainties of 3.5% and 6.0% in the general flux calibration for 2.0 mm and 1.25 mm, respectively. These numbers are derived from the variations in the Uranus fluxes during the observing run containing our target observations, and are in line with the typical values reported in Perotto et al. (2020).